In vivo quantitative analysis of *Caulobacter crescentus* Z-ring organization by high throughput 3D PALM

Seamus J. Holden[1*], Thomas Pengo[1], Karin Meibom[1], Carmen Fernandez-Fernandez[2], Justine Collier[2], Suliana Manley[1*]

[1]Laboratory of Experimental Biophysics, École Polytechnique Fédérale de Lausanne (EPFL), Switzerland
[2]Department of Fundamental Microbiology, Faculty of Biology and Medicine, University of Lausanne, Switzerland
[*]To whom correspondence should be addressed. Email: seamus.holden@gmail.com or suliana.manley@epfl.ch.

Supplementary information

Video S1:

3D volume and isosurface rendering of a patchy early pre-divisional Z-ring. Video shows same cell as Fig. 3Aiv.

Video S2:

3D volume and isosurface rendering of a complete early pre-divisional Z-ring. Video shows same cell as Fig. 3Av.

Video S3:

3D volume and isosurface rendering of an incomplete mid/ late pre-divisional Z-ring, #1. Video shows same cell as Fig. 3Bii.

Video S4:

3D volume and isosurface rendering of an incomplete mid/ late pre-divisional Z-ring, #2. Video shows same cell as Fig. 3Biv.

Video S5:

3D volume and isosurface rendering of a Z-ring for an SOS-induced cell, #1. Video shows same cell as Fig. S12A.

Video S6:

3D volume and isosurface rendering of a Z-ring for an SOS-induced cell, #2. Video shows same cell as Fig. 12B.

Video S7:

Timelapse phase contrast imaging of cells in the presence of 0.8 μg/ mL mitomycin C.

Supplementary Methods

***C. crescentus* strains and plasmids.** An integrating plasmid containing *ftsZ-dendra2* under a xylose-inducible promoter (1) was introduced into the CB15N wild-type *C. crescentus* strain by transformation, producing a merodiploid strain containing both the *ftsZ* gene and a single chromosomal copy of *ftsZ-dendra2* under the control of the native *xylX* promoter. The plasmid pXC2-*ftsZ-dendra2* (1) was electroporated into the strain CB15NΔ*lexA* (2) to construct a *ΔlexA Pxyl::ftsZ-dendra2* strain.

Sample preparation. *HTPALM synchrony.* Liquid cultures of the *Pxyl::ftsZ-dendra2* strain in M2G media (3) were grown overnight to early-exponential phase. 0.003% xylose was added, and the cells were grown for 3 hrs to mid-exponential phase (~OD 0.4). Cultures were placed on ice, swarmer cells were isolated via Percoll density centrifugation (synchronized (4)) and resuspended to ~OD 1.0 in cold M2G. 5 uL of culture was placed on a room temperature 2.5% agarose pad, containing M2G and 0.003% xylose. The agarose pad was mounted in a silicone gasket (Grace Biolabs 103280) on top of a microscope coverslip. After 1 min incubation, the agarose pad was sealed with a plasma-cleaned microscope coverslip. The sealed silicone gasket largely eliminated shrinkage and drying of the agarose pad over the timescale of the experiment. The time when the culture was added to the room temperature agarose pad was counted as t=0 min for the synchrony. The temperature of the microscope enclosure during experiments was 24°C. *HTPALM, asynchronous cells, higher induction level.* Liquid cultures of the *Pxyl::ftsZ-dendra2* strain in M2G media (3) were grown overnight to early-exponential phase. 0.015% xylose was added, and the cells were grown for 3 hours to mid-exponential phase (~ OD 0.4). 1 mL of culture was centrifuged and resuspended to ~ OD 1.0 in room temperature M2G. 5 uL of culture was immobilized on an agarose pad containing M2G and 0.015 % xylose, and immobilized and imaged as above. *HTPALM during DNA damage conditions.* Cultures of the *ΔlexA Pxyl::ftsZ-dendra2* strain were grown, induced with 0.003% xylose for 3 hours and synchronized by density centrifugation as described above. 5 µL of culture was immobilized on an agarose pad containing M2G, 0.003 % xylose, and 0.8 µg/ mL mitomycin C (Sigma M0503), and immobilized and imaged as above. Timelapse phase contrast imaging of unsynchronized cells in the presence of M2G (Video S7) showed that cells either continued to elongate for > 10 hrs, showing that cells were alive at the time of HTPALM imaging, or failed to elongate from the beginning of the measurement; these cells (short swarmer cells in the case of the synchronized HTPALM experiment) were excluded based on length. *Imaging of FtsZ in lexA-deficient bacteria.* The strain was grown in M2G medium to early exponential phase. Expression of *ftsZ-dendra2* was induced by addition of 0.003% xylose. After 3 hours of induction in liquid media, bacteria were placed on M2G agarose pads containing 0.003% xylose, and incubated at room temperature for 5 hours. Bacteria were then immobilized and imaged as above.

HTPALM hardware. Imaging was performed on a custom built microscope, designed for stability and automation. Cells were imaged with an NA 1.49 oil immersion objective lens (Nikon), and fluorescence was detected using a 128x128 pixel EMCCD camera (Photometrics Evolve 128). Fluorescence was excited at 560 nm (MPB VFL-P-300-560), and photoactivation was induced at 405 nm (Coherent OBIS) at ~ 0-16 W/ cm^2. Cells were imaged at an exposure time of 10 ms for 80 s, with an excitation intensity at 560 nm of 4 kW/ cm^2, except for the reduced acquisition time dataset (Figure S8), where cells were imaged at an exposure time of 5 ms for 20 s, with an excitation intensity at 560 nm of 8 kW/ cm^2.

Computer control of laser power was implemented using a combined DAC/ TTL controller (ESio AOTF controller). Laser light was reflected off a four-color dichroic mirror (Chroma ZT405/488/561/640rpc) and directed upon the sample in a highly inclined, near-TIRF mode to minimize background autofluorescence (5). Light reaching the EMCCD passed through the dichroic mirror and an emission filter (Chroma ET605/52m).

Mechanical drift was minimized by mounting the objective in a solid block of aluminum, attached to the microscope frame (ASI RAMM), rather than mounting it on a moveable turret. Sample z-position

was controlled using a 500 um travel z-piezo stage (ASI PZ-2500). Sample xy-position was controlled using an automated servo motor stage (ASI). Thermal stability was achieved by placing all of the imaging components of the microscope in a thermally insulated enclosure, with the major heat sources (lasers, liquid cooling for EMCCD) placed outside of the enclosure. Further Z-axis stabilization was performed using a commercial autofocus device (ASI CRIFF), which measures and maintains a constant objective-coverslip separation based on the reflected position of an 850 nm LED. 850 nm light from the CRIFF was directed onto the sample, and also collected, using an 805 nm short pass dichroic mirror (Thorlabs DMSP805R), placed immediately behind the objective, before the imaging optics. Drift on the microscope over 80 s was 6 nm in xy and 22 nm in z, based on the standard deviation of the localized position of 100 nm fluorescent beads (Invitrogen TetraSpeck) adsorbed to glass.

Brightfield illumination for phase contrast imaging consisted of a white LED (Thorlabs MCWHL2), passed through a green filter (Chroma ET525/50mc), focused into the back focal plane (BFP) of a condenser lens (Nikon MEL56100). A phase annulus (Nikon MEH54340) was placed in the condenser BFP. 10 % of the light exiting the objective lens was collected via a 10/ 90 beamsplitter (Chroma 21012) placed behind the autofocus dichroic and in front of the fluorescence dichroic. This 10 % of light was directed to the external phase contrast pathway. A 4f-system was implemented, so that the light was refocused into a conjugate BFP, where a phase ring (Nikon MEH55940) was mounted, before finally being directed onto a 1024x768 CMOS camera (The Imaging Source DMK 31BU03).

3D-PALM was implemented using astigmatic imaging (5), by placing a 1 m focal length cylindrical lens (Thorlabs LJ1516RM-A) 90 mm in front of the image plane.

The phase contrast and fluorescence channels were coaligned by taking sequential images of a 0.5 μm fluorescent bead (Invitrogen TetraSpeck), evenly spaced in 1.5 μm steps across the field of view. This was used to generate an alignment transform using the local weighted mean algorithm (6).

HTPALM software. HTPALM data acquisition control was implemented as a plugin to *MicroManager* (7). This plugin performs automated PALM imaging of hundreds of fields of view (FOVs), acquiring data only for FOVs containing sufficient numbers of cells. The software searches for immobilized cells on the sample using the phase contrast imaging channel. Cells are counted by removing uneven background illumination using a high-pass filter, segmenting the image with Otsu's method, and counting the number of cells whose area is within user-defined size limits. If an FOV is found to contain a number of cells within the user-defined range, an acquisition is initiated. Each acquisition consists of a pre-acquisition phase contrast image, a PALM movie, and a post-acquisition phase contrast image.

During PALM imaging, the density of active fluorophores is controlled by real-time image analysis and closed-loop control of the photoactivation laser (Supplementary Note 1, Fig. S2). This is performed using a separate MicroManager plugin, called *AutoLase*. Because *AutoLase* is a separate plugin to the HTPALM software, it is straightforward to install and run separately, so that automatic photoactivation control can be easily implemented even for regular PALM measurements.

Briefly, we estimate the amount of time that each pixel in an image has been continuously bright (above-threshold). Because single fluorophores have a characteristic on-time, whereas regions containing many bright fluorophores will remain bright for much longer, we can optimize the on-time of pixels in the image (precisely, the *N*-frame smoothed maximum on-time) by closed loop adjustment of the photoactivation laser. Since this algorithm does not require real-time localization, but instead only a simple image segmentation operation, it is not computationally intensive and does not require special hardware such as GPU arrays to run. Also, whereas localization-based methods (8) will fail at identifying high-density regions of active fluorophores unless they are specially designed (9), high densities of active fluorophores will simply give longer on-times in *AutoLase*; this should make the algorithm robust at high density.

HTPALM data analysis. 3D-PALM localization was performed using RapidStorm3.2 (10), running in batch mode. PALM localizations were corrected for refractive index mismatch by rescaling the z-values by a factor of 0.72 (11). Despite refractive index mismatch correction, z-ring cross-section images were observed to be uniformly slightly asymmetric along the z-axis (5 %, manual estimate, *n=21*). This most likely does not correspond to actual z-ring asymmetry, rather it probably reflects uncertainty in the calculation of the z-axis correction factor (11), eg. due to uncertainty in the refractive index of the imaging medium (liquid/ agarose interface) or the variation in refractive index in the bacterial cytoplasm relative to the imaging medium (12).

PALM localizations were transformed into the coordinate system of the phase contrast channel using the previously generated alignment transform (see *HTPALM hardware*, above). *Xy*-drift during image acquisition (20 nm on average), largely due to contraction of agarose, was corrected for by cross-correlating the pre- and post-phase images to estimate the drift between the first and last frames of the PALM acquisition, and applying a linear correction.

The pre-acquisition phase contrast image was analyzed using a slightly modified version of MicrobeTracker (13) to generate cell outlines. The main modification was to allow script-based operation of MicrobeTracker, so that it could be incorporated into our software; additionally, minor modifications to image background subtraction and segmentation were made to improve robustness. Erroneously segmented cells were rejected based on length, maximum width, and integrated curvature; the top and bottom 3-5% of cells were excluded for each of these parameters (grey circles, Fig. S11). For synchronies, cells which failed to elongate were excluded (orange circles, Fig. S11). Also for synchronies, the lengths of the remaining cells were plotted against time of acquisition, and a linear fit performed. Cells with a length further than 1.5 standard deviations from the linear fit were excluded to maximize synchronization (black lines, Fig. S11). Figure S11 shows the results of these filtering operations, and illustrates the degree of variation in cell length (and thus synchronization) on remaining cells. After these filtering operations, few erroneous segmentations were observed; a manual analysis of 285 automatically segmented bacteria revealed only 10 erroneous segmentations (4 %).

For DNA damage measurements (MMC treated cells and *ΔlexA* cells), the high degree of filamentation was problematic for the automated filtering method. Therefore, poorly segmented cells were manually excluded for these datasets.

Finally, PALM localizations in the region of a cell were placed into the internal coordinate system of that cell; ie. the distance of each localization along the cell centerline and displacement off the cell centerline were calculated.

HTPALM data acquisition and analysis source code and executables will shortly be made available; please see the Manley laboratory website, http://leb.epfl.ch/software.

Image rendering. PALM images were rendered by binning localizations with a pixel size of 10 nm, and Gaussian blurring the image using a FWHM of 35 nm (corresponding to *xy* localization precision). PALM image intensities were normalized, but were not contrast saturated. *Z*-cross sections were plotted in the *zd* coordinate system, where *d* is lateral displacement from cell mid-plane in transformed xy coordinates. This removed the effect of cell curvature; in effect the cell is artificially straightened out, facilitating automated identification and plotting of the z-ring along a cross-section perpendicular to the cell axis. This was achieved using the "internal" bacterial coordinate system, established using the cell outline measured from the phase contrast image (13).

Spatial resolution. The mean photon count/ molecule/ frame for Dendra2 for an exposure time of 10 ms and an excitation power of 4 kW/ cm^2 was 230 photons/ molecule/ frame. Localization precision was estimated experimentally based on the localization uncertainty of 100 nm beads adsorbed to glass, illuminated at an intensity to give approximately the same photon emission rate as Dendra2, imaged at the same exposure time (10 ms); we observed a localization precision (standard

deviation of observed localizations) of 15 nm in *xy* and 50 nm in *z*. The spatial resolution (14), ie. the minimum resolvable separation of two objects, is more readily interpreted, and is easier to compare to other (non-localization-based) microscopies; therefore we use this metric throughout the main text (except in discussion of Ref. (15), whose authors quote localization precision only). The spatial resolution is equal to the FWHM of the localization precision (2.35 times the standard deviation for a Gaussian distribution). The spatial resolution of our measurement was 35 nm in *xy* and 120 nm in *z*.

For the reduced acquisition time dataset, with an exposure time of 5 ms and an excitation power of 8 kW/ cm^2, the photon count was ~ 200 photons/ molecule/ frame, very similar to the previous condition, meaning that the spatial resolution was approximately the same as above (35 nm in *xy* and 120 nm in *z)*.

Nyquist resolution analysis. Nyquist-limited resolution (16) was estimated as per (17). Z-cross-sections were segmented using Otsu's method, and the number of localizations within the segmented area was calculated. Nyquist resolution is the resolution at which there are at least two localizations per pixel on average, ie. $r_{nyq} = 2/\sqrt{n/A}$ (17), where *n* is the number of localizations and *A* is the area of the segmented region. The Nyquist resolution for all 292 Z-cross-sections of the dataset shown in Fig. 3 was 17 ± 8 nm (mean ± s.d.). The Nyquist resolution for all Z-cross-sections for the dataset shown in Fig. S8 (with each image acquired in 20s) was 42 ± 18 nm (mean ± s.d.).

Measurement of number of localized molecules. The number of localized molecules was estimated by grouping localizations from fluorophores which remained continuously on for several frames (ie. localizations present in adjacent frames within a radius of 50 nm) as per Ref. (18). Table S1 presents the number of localized molecules for each dataset and image, which shows that all images and calculations are based on well-sampled data. ***NB:*** *These numbers do not represent accurate estimates of the total amount of labelled FtsZ in the cell.* Molecules were not counted exhaustively for each cell (since this would require excessively long acquisition time). If molecules are not counted exhaustively, molecule counts depend on the photoactivation rate in each experiment, and on the projected 2D area of a structure. For example, the large extended rings observed for the MMC condition show higher a higher number of observed molecules per ring than untreated cells (Table S1) due to their larger area, but since molecules were not counted exhaustively, this does not prove that they contain a larger total number of molecules.

3D volume rendering. Localizations were binned in 3D using a voxel size of 10 nm, Gaussian blurring in *xy* with a FWHM of 35 nm (*xy* spatial resolution), and blurring in *z* with a FWHM of 120 nm (*z* spatial resolution). A density iso-surface was calculated in an unbiased fashion using Otsu's method (19); the resulting 3D surface was then plotted. Figures were 3D-rendered using MATLAB (Mathworks, USA). Videos were rendered using Imaris (Bitplane, UK).

Quantitative analysis of Z-ring morphology. Manual checking of the xy-images revealed that a small number of cell outlines were erroneously segmented (10 of 285 cells); these were excluded from analysis. For each cell, the brightest 250 nm region along the cell centerline was automatically identified (corresponding to the Z-ring position), and a z-cross-section image was rendered, as above.

Z-ring morphology classification. Each image was segmented using Otsu's method (19), giving a binary cross-section image with pixels containing significant FtsZ localizations being above threshold. The binary image was dilated with a 3x3 structuring element in order to connect regions which were "almost" connected (ie. only connected by pixel corners). Each binary image was manually classified as *disc/ spot* (Fig. S7Ai, Bi, ellipsoid containing no holes), *patchy* (Fig. S7Aii, Bii, discontinuous annulus with all arcs < 180°), *incomplete ring* (Fig. S7Aiii, Biii, discontinuous annulus with an arc > 180°), or *ring* (Fig. S7Aiv, Biv, continuous annulus). In ambiguous cases (eg. distinguishing between small patches and small spots), the original *xy* and *z*-cross-section images were consulted to confirm the morphology.

Ring diameter. Ring diameter was measured for 263 bacteria by manually measuring a best fitting circle along the z-cross-section image, since automated estimates were found to perform poorly for asymmetric patchy rings. A small number of bacteria (12 of 275) for which the radius could not be clearly estimated were excluded from the analysis. Two exemplar manual estimates of z-ring radius are shown Fig. S9A. Due to the reduced spatial resolution along the z-axis, and also the small amount of z-axis distortion, the xy-axis was manually given greater weight during the visual estimation of z-ring radius (eg. Fig. S9Ai).

Z-ring thickness. Axial Thickness. Axial Z-ring profiles for the same 263 bacteria were measured along a 50 nm thick representative cross-section, as near to the cell centerline as possible. In order to avoid smearing effects from the overlapping of the top and bottom of a Z-ring, only the thickness of either the top half or the bottom half of the Z-ring was measured. *Ie.* if a Z-ring filament was only present either in the top part, or the bottom part of the mid-cell constriction, that part was measured. In the (less common) case of quite continuous rings containing significant localizations at the top and bottom of the constriction, whichever half contained more localizations was analyzed. *Radial thickness.* Radial Z-ring profiles for the 141 bacteria showing a non-spot morphology were measured along a 50 nm thick cross-section, as near as possible parallel to the horizontal axis, in order to exploit the higher *xy* resolution of 35 nm, rather than the lower 120 nm *z* resolution. Axial and radial thickness was measured by calculating the FWHM of a 1D Gaussian fitted to the profile. Exemplar axial and radial thickness measurements are shown in Fig. S9B-C.

Z-ring volume. Z-ring isosurfaces were automatically calculated using Otsu's method, as described in *"3D volume rendering"*. The total ring volume was calculated by counting number of voxels within this isosurface (ie. the number of voxels with an above threshold intensity value), and multiplying by the volume of a single voxel (10^{-6} μm^3). Since the observed volume distributions were observed to be non-Gaussian (Fig S12C, skewed and containing outliers), statistical comparison of the medians (rather than the averages) was performed using the Mann-Whitney-Wilcoxon test. Significance was assessed at the $p < 0.05$ level.

Estimation of onset of membrane constriction. In order to estimate the onset of membrane constriction post-synchrony, phase contrast images of each cell were manually inspected for the presence of visible mid-cell invagination (*n =275)*; the percentage of cells showing invagination was then calculated over 50 min intervals (Figure S10).

Western Blotting. CB15N and *Pxyl::ftsZ-dendra2* strains were grown to early exponential phase and xylose was added to final concentration of 0%, 0.003% or 0.015%. After an additional two hours growth, bacteria were pelleted and resuspended and lysed directly in Laemmli buffer. Proteins were resolved on 10% SDS-PAGE and electrotransferred to a nitrocellulose membrane (Hybond ECL, GE Health Sciences). Immunodetection was performed using polyclonal antibody against FtsZ and an anti-rabbit antibody conjugated to horseradish peroxidate (Sigma Aldrich) at 1:10,000 dilutions as previously described (20). Chemiluminescence detection was performed using the ECL kit (Pierce) according to the instructions from the manufacturer. Image processing and measurements of relative band intensities were performed using Fiji (21).

Supplementary Note 1: Automated closed-loop feedback control of the density of active fluorophores during PALM.

In order to perform localization microscopy, a careful balance in the density of bright fluorescent molecules (imaging density) is required: if imaging density is too high, spatial resolution is reduced; if imaging density is too low, temporal resolution is reduced. In PALM (22) and STORM (23), the imaging density is usually sensitive to the illumination intensity of a "photoactivation" UV laser (22, 23). The imaging density can thus be adjusted to its optimal level by changing the photoactivation laser power (hereafter, UV power). However, the UV power required to maintain optimal imaging density will vary significantly during a measurement, due to irreversible photobleaching of an

increasing fraction of the fluorophores as the experiment progresses. It will also vary significantly between different fields of view within a sample, e.g. due to variations in the morphology and labeling density of the labeled structure.

Imaging density is usually controlled by continuous manual assessment of the density of molecules in any single frame, and manual adjustment of UV power. This is tedious, and most importantly, is incompatible with automation. As part of the HTPALM method, we therefore designed *AutoLase*, an algorithm for measurement and closed-loop feedback control of imaging density.

One possible approach (8) is to perform real-time localization analysis as the data is acquired and optimize the UV power based on the observed number of localizations. However, this approach has two main limitations. First, real-time localization is computationally intensive; it will therefore be difficult to implement for high frame-rate imaging and/ or for large field of view cameras (e.g. sCMOS cameras). Second, localization will fail at high imaging density, since multiple overlapping PSFs will be erroneously grouped together unless high-density fitting algorithms (9) (which are currently too slow for real-time analysis) are used.

The design requirements for AutoLase were thus low computational burden and good performance at high imaging density. Instead of trying to optimize sampling rate using only the information from an individual frame, the problem can be significantly simplified by including temporal information from multiple frames. The amount of time that individual fluorophores remain in a bright, photon emitting state is Poisson distributed about a mean lifetime τ_{on}. Therefore, any region of a sample which remains continuously bright for significantly longer than τ_{on} very likely contains multiple bright fluorophores instead of just one. We devised an image-based estimator of τ_{on}, by estimating the amount of time that each pixel in an image has been continuously bright. This allows us to estimate the number of bright molecules, without the need for real-time localization. Since τ_{on} will increase with the number of active bright molecules, this estimator will be robust at high imaging density.

For each frame *k*, and for each pixel *i*, we define the estimated on-time, $\tau_{i,k}$,

$$\tau_{i,0} = 0,$$
$$\tau_{i,k} = (\tau_{i,k-1} + \Delta t)\ M_{th}(I_i),$$

where Δt is the interval between each frame, I_i is the intensity at the current pixel, *th* is an intensity threshold, and $M_{th}(I)$ is the binary threshold operator,

$$M_{th}(I) = \begin{cases} 1 & \text{if } I \geq th, \\ 0 & \text{otherwise.} \end{cases}$$

Each time the pixel intensity I_i falls below *th*, $\tau_{i,k}$ is set to *0*. If I_i is above threshold, $\tau_{i,k}$ is equal to the duration for which that pixel has been above threshold at frame *k*. τ is thus a measure of how long each pixel has been *continuously* bright.

We implemented closed-loop feedback control of τ. The maximum value of τ at each frame *K* is smoothed via a running mean

$$\tau_{max} = \frac{1}{N} \sum_{K-N+1}^{K} \max_i\ \tau_{i,k},$$

and compared to a target value *T*. If the observed value of τ is above or below *T* by more than *x* %, then the UV power is reduced or increased, respectively. We calculated the image maximum of τ rather than an average. We reasoned that although the maximum is more noisy than the average, the

key criterion is that there are no "hot-spots", ie. that there are not small regions of the image which contain too many active molecules.

Closed-loop feedback control was implemented on our HTPALM microscope, controlled using the open-source instrument control software, Micromanager (7). We wrote a plugin to Micromanager, called *AutoLase*, to perform the feedback control, which we will shortly release as open-source software. Because Micromanager is open-source and works for a large variety of instruments, and because *AutoLase* is not computationally intensive and does not require real time localization analysis, it should be straightforward for researchers to implement feedback control on their own systems using our software.

The performance of the *AutoLase* algorithm in estimating τ_{on} is shown in Fig. S2. Live *C. crescentus* bacteria expressing FtsZ (1) were imaged at a frame rate of 100 Hz using *AutoLase* to control the imaging density. An exemplar subset of frames (Fig. S2A) shows the blinking behavior of the labeled molecules. Most fluorophores remain bright for less than 100 ms, however, two fluorophores (top middle and top right of images) remain bright for greater than 200 ms. The on-time estimator τ successfully captures this behavior (Fig. S2B), showing only two regions active for greater than 200 ms, consistent with the visual interpretation of the raw data.

AutoLase feedback control is shown in Fig. S2C-D. With feedback control (Fig. S2C), the laser power was initially 0 %, and *AutoLase* was turned on at t=0 s. The raw τ_{max} data is quite noisy (grey line), but clear trends are visible in the calculated running mean (black line). Before t=0 s, most molecules are in their dark state, with only occasional spikes in τ_{max} due to autofluorescence or photoactivation by the imaging laser. When *AutoLase* is turned on at t=0 s, the laser power (blue line) is rapidly increased and stabilizes at ~10 % for the first 50 s of imaging, after which point it increases in approximately exponential form to the maximum user-defined power. This produces observed on-times stable around the target value of 400 ms for nearly 100 s, after which τ_{max} gradually decreases because very few unbleached molecules remain.

To compare performance without feedback control (Fig. S2D), a new field of view (FOV) was chosen, and the laser power was set to 10 % of maximum power at t=0 s, since this was observed to be the stable initial value for the previous FOV. Interestingly, this power level produces an observed τ_{max} well above the target value of 400 ms for the first 50 s of imaging. This is presumably due to variation in density of labeled molecules between different FOVs. Between 50-100 s, τ_{max} is near the target value, after which it decreases rapidly.

These results show that *AutoLase* can rapidly and accurately optimize τ_{max} to a given target value, and that this value can be maintained for extended periods of time. By contrast, setting the power to a constant value without feedback control is sensitive to variations in density of labeled molecules, which occurs even between adjacent FOVs (e.g. due to variation in morphology of the labeled structure), and significantly reduces the period for which τ_{max} is close to the target value. In practice, we have found that *AutoLase* gives performance at least as good as manual optimization of the UV power, whilst also being compatible with automated PALM imaging.

Supplementary References

1. Biteen JS, Goley ED, Shapiro L, Moerner WE (2012) Three-dimensional super-resolution imaging of the midplane protein FtsZ in live Caulobacter crescentus cells using astigmatism. *ChemPhysChem* 13:1007–1012.

2. Da Rocha RP, de Miranda Paquola AC, do Valle Marques M, Menck CFM, Galhardo RS (2008) Characterization of the SOS Regulon of Caulobacter crescentus. *J Bacteriol* 190:1209–1218.

3. Ely B (1991) in *Methods in Enzymology*, ed Jeffrey H. Miller (Academic Press), pp 372–384.

4. Alley MRK (2001) The highly conserved domain of the Caulobacter McpA chemoreceptor is required for its polar localization. *Mol Microbiol* 40:1335–1343.

5. Huang B, Wang W, Bates M, Zhuang X (2008) Three-Dimensional Super-Resolution Imaging by Stochastic Optical Reconstruction Microscopy. *Science* 319:810–813.

6. Churchman LS, Spudich JA (2012) Colocalization of Fluorescent Probes: Accurate and Precise Registration with Nanometer Resolution. *Cold Spring Harb Protoc* 2012:pdb.top067918.

7. Edelstein A, Amodaj N, Hoover K, Vale R, Stuurman N (2010) in *Current Protocols in Molecular Biology*, eds Ausubel FM et al. (John Wiley & Sons, Inc., Hoboken, NJ, USA).

8. Kechkar A, Nair D, Heilemann M, Choquet D, Sibarita J-B (2013) Real-Time Analysis and Visualization for Single-Molecule Based Super-Resolution Microscopy. *PLoS ONE* 8:e62918.

9. Holden SJ, Uphoff S, Kapanidis AN (2011) DAOSTORM: an algorithm for high- density super-resolution microscopy. *Nat Meth* 8:279–280.

10. Wolter S et al. (2012) rapidSTORM: accurate, fast open-source software for localization microscopy. *Nat Methods* 9:1040–1041.

11. Huang B, Jones SA, Brandenburg B, Zhuang X (2008) Whole-cell 3D STORM reveals interactions between cellular structures with nanometer-scale resolution. *Nat Meth* 5:1047–1052.

12. Valkenburg JA, Woldringh CL (1984) Phase separation between nucleoid and cytoplasm in Escherichia coli as defined by immersive refractometry. *J Bacteriol* 160:1151–1157.

13. Sliusarenko O, Heinritz J, Emonet T, Jacobs-Wagner C (2011) High-throughput, subpixel precision analysis of bacterial morphogenesis and intracellular spatio-temporal dynamics. *Mol Microbiol* 80:612–627.

14. Bates M, Huang B, Dempsey GT, Zhuang X (2007) Multicolor Super-Resolution Imaging with Photo-Switchable Fluorescent Probes. *Science* 317:1749–1753.

15. Biteen JS, Goley ED, Shapiro L, Moerner WE (2012) Three-Dimensional Super-Resolution Imaging of the Midplane Protein FtsZ in Live Caulobacter crescentus Cells Using Astigmatism. *ChemPhysChem* 13:1007–1012.

16. Shroff H, Galbraith CG, Galbraith JA, Betzig E (2008) Live-cell photoactivated localization microscopy of nanoscale adhesion dynamics. *Nat Meth* 5:417–423.

17. Shim S-H et al. (2012) Super-resolution fluorescence imaging of organelles in live cells with photoswitchable membrane probes. *Proc Natl Acad Sci* 109:13978–13983.

18. Puchner EM, Walter JM, Kasper R, Huang B, Lim WA (2013) Counting molecules in single organelles with superresolution microscopy allows tracking of the endosome maturation trajectory. *Proc Natl Acad Sci*:201309676.

19. Otsu N (1979) A Threshold Selection Method from Gray-Level Histograms. *IEEE Trans Syst Man Cybern* 9:62–66.

20. Gonzalez D, Collier J (2013) DNA methylation by CcrM activates the transcription of two genes required for the division of Caulobacter crescentus. *Mol Microbiol* 88:203–218.

21. Schindelin J et al. (2012) Fiji: an open-source platform for biological-image analysis. *Nat Methods* 9:676–682.

22. Betzig E (2006) Imaging intracellular fluorescent proteins at nanometer resolution. *Science* 313:1642–1645.

23. Rust MJ, Bates M, Zhuang X (2006) Sub-diffraction-limit imaging by stochastic optical reconstruction microscopy (STORM). *Nat Methods* 3:793–795.

Supplementary Figures

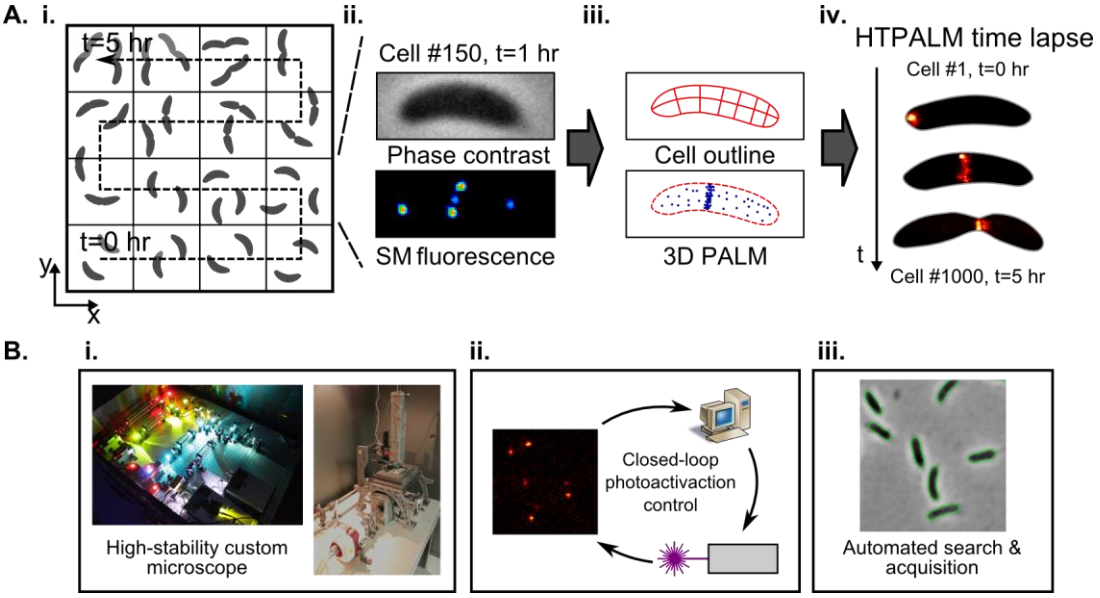

Figure S1: *HTPALM schematic*. *A. i-ii.* PALM and phase contrast (PH) images are automatically acquired for many fields of view, as the cell cycle progresses in a synchronized bacterial population. Fields of view acquired later in the experiment contain bacteria in later stages of the cell cycle. *iii.* Single molecule localizations are extracted from the PALM images, and cell outlines are extracted from the PH images. *iv.* Data is combined to produce a HTPALM time lapse showing super-resolved changes in single molecule localization over the whole cell cycle. *B.* HTPALM is facilitated by (i) a high-stability home-built microscope, which significantly reduces drift, (ii) closed-loop control of the density of bright fluorophores, and (iii) custom software to automatically search for bacteria and record PALM and PH images.

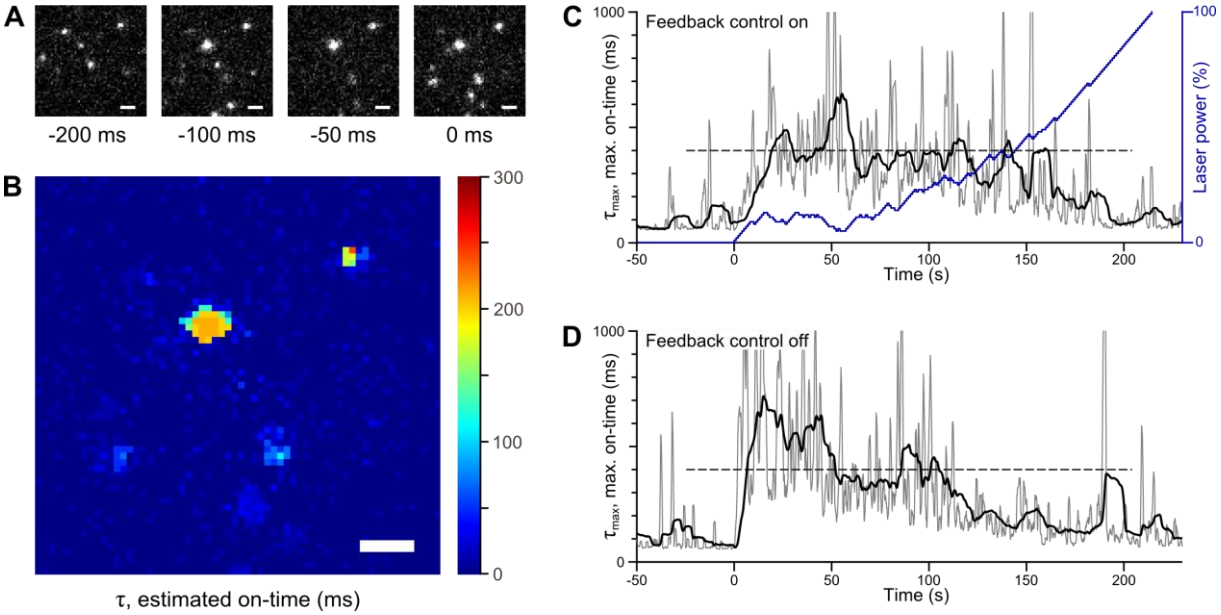

Figure S2: *Measurement and control of molecule on-time using AutoLase. A.* Exemplar subset of images of live *C. crescentus* expressing FtsZ-Dendra2, under photoswitching conditions. *B*. Estimated on-time for each pixel, for frame corresponding to t = 0 ms in A. *C-D.* Observed maximum single-pixel on-time (τ_{max}), with (C) and without (D) feedback control. Raw data, gray line; smoothed data, black line; laser power, blue line. For the case with feedback control turned off (D), UV power was set to 10 % at t= 0 s. Scale bars, 1 µm.

Phase contrast images, corresponding to main text figures.

Figure 2

Figure 3

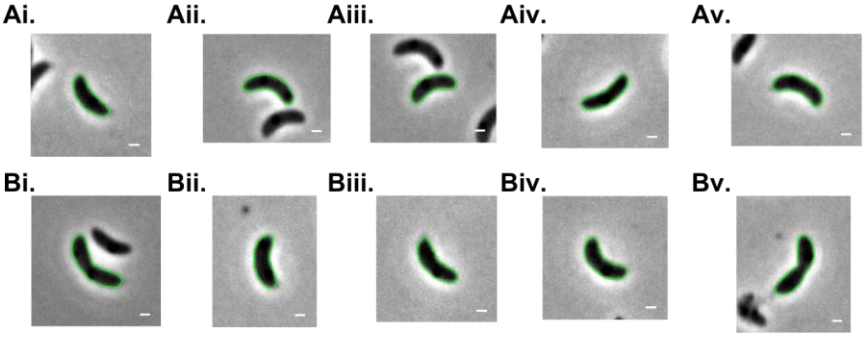

Figure S12

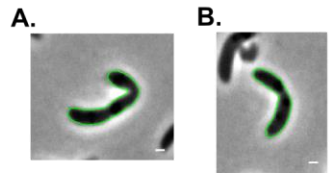

Figure S3: *Phase contrast images of cells shown in Fig. 2., Fig. 3, and Fig. S12.* Green line, automatically calculated cell outline. PALM images have been rotated relative to the phase contrast images. Scale bars, 500 nm

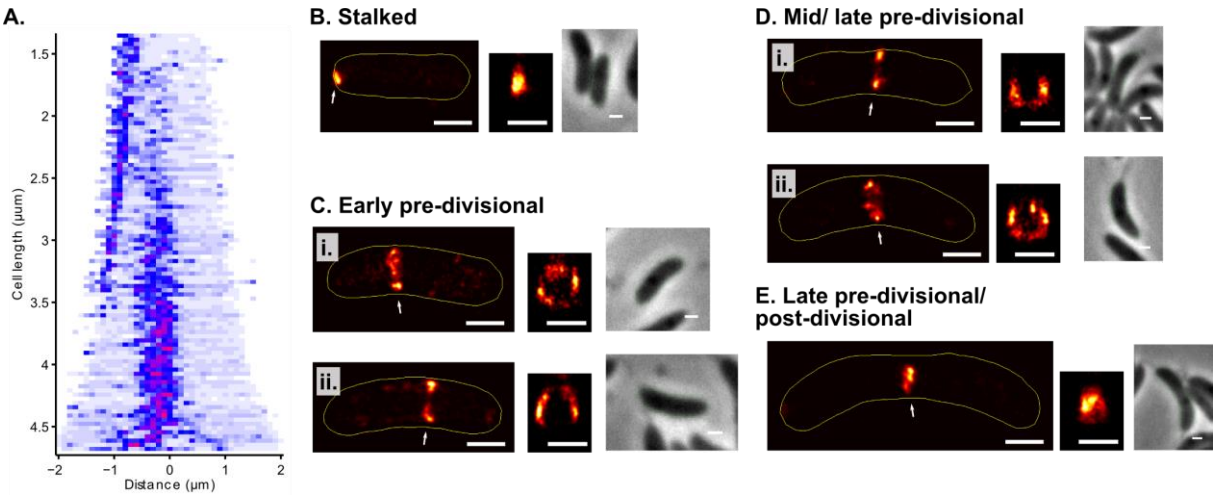

Figure S4: *Increasing the FtsZ-Dendra2 expression level does not alter ring morphology.* Induction level, 0.015% xylose (5x higher than for data shown in Figure 2). *A.* FtsZ localization along the cell as a function of cell length, for 889 cells. *B-E.* Representative PALM images of FtsZ localization throughout cell cycle, in xy (left) and in *zd* cross-section (right), where *d* is lateral displacement from cell mid-plane. Yellow line indicates cell outline, automatically determined from a phase contrast image. Arrow indicates region shown in z-cross-section. Corresponding phase contrast image for each cell is also shown. Green line indicates cell outline. PALM images have been rotated relative to the phase contrast images. Scale bars, 500 nm.

A.

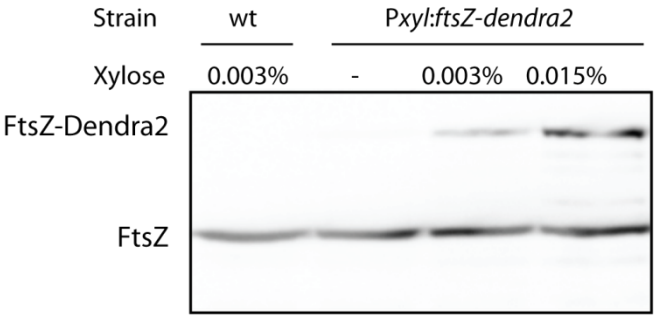

B.

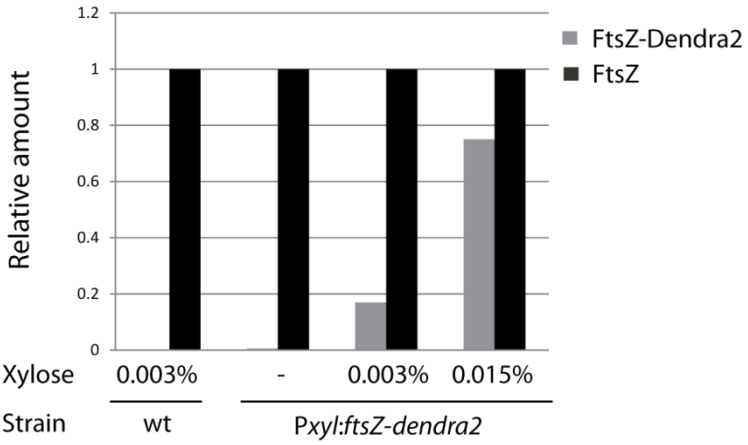

Figure S5: *Comparison of the protein levels of FtsZ and FtsZ-Dendra2.* A. Immunoblot analysis using polyclonal anti-FtsZ after growth with the inducer xylose at various concentrations for two hours. B. Relative amounts of FtsZ and FtsZ-Dendra as determined from the band intensities. Exact percentages of FtsZ-Dendra2 in each lane: 0%, 0.6%, 17%, 75% relative to native FtsZ.

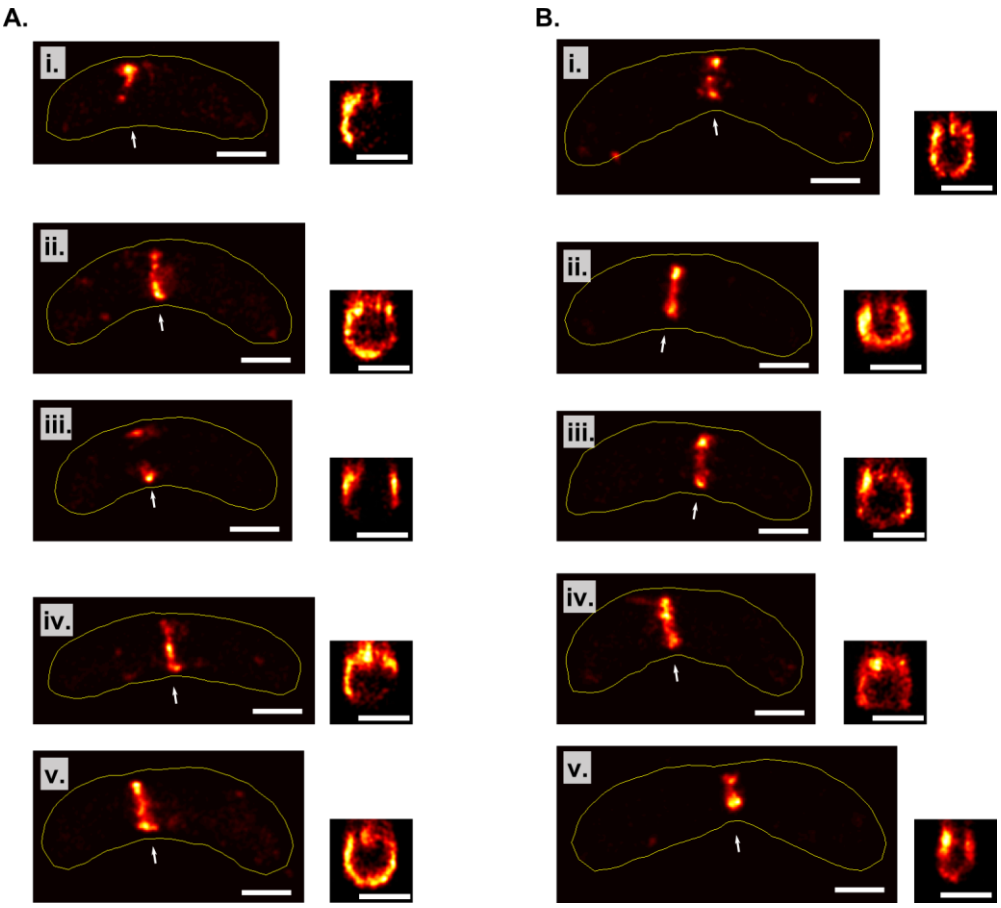

Figure S6: *Z-ring cross-sections & xy cell images for 3D volume renderings shown in Fig. 3. Yellow outline:* automatically calculated cell outline. *White arrow* indicates region of *z* cross-section. Scale bars, 500 nm.

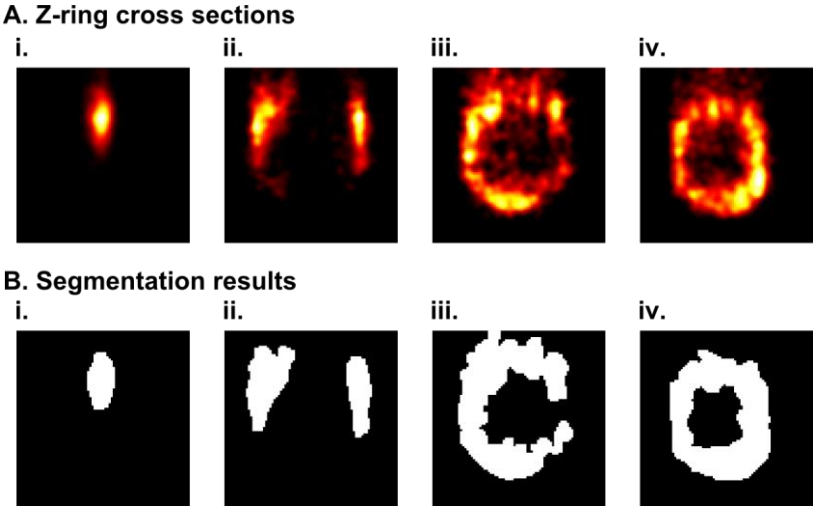

Figure S7: *Examples of ring classification for Z-ring morphology analysis (Fig 4A). A.* Z-ring cross-sections are automatically calculated and plotted for each bacterium in the dataset. *B.* Cross-sections are segmented using Otsu's method, and dilated using a 3x3 structuring element, and manually classified into one of four Z-ring morphology classes: *disc/ spot* (A.i, B.i, ellipsoid containing no holes), *patchy* (A.ii, B.ii, discontinuous annulus with all arcs < 180°)*, incomplete ring* (A.iii, B.iii, discontinuous annulus with an arc > 180°), or *ring* (A.iv, B.iv, continuous annulus).

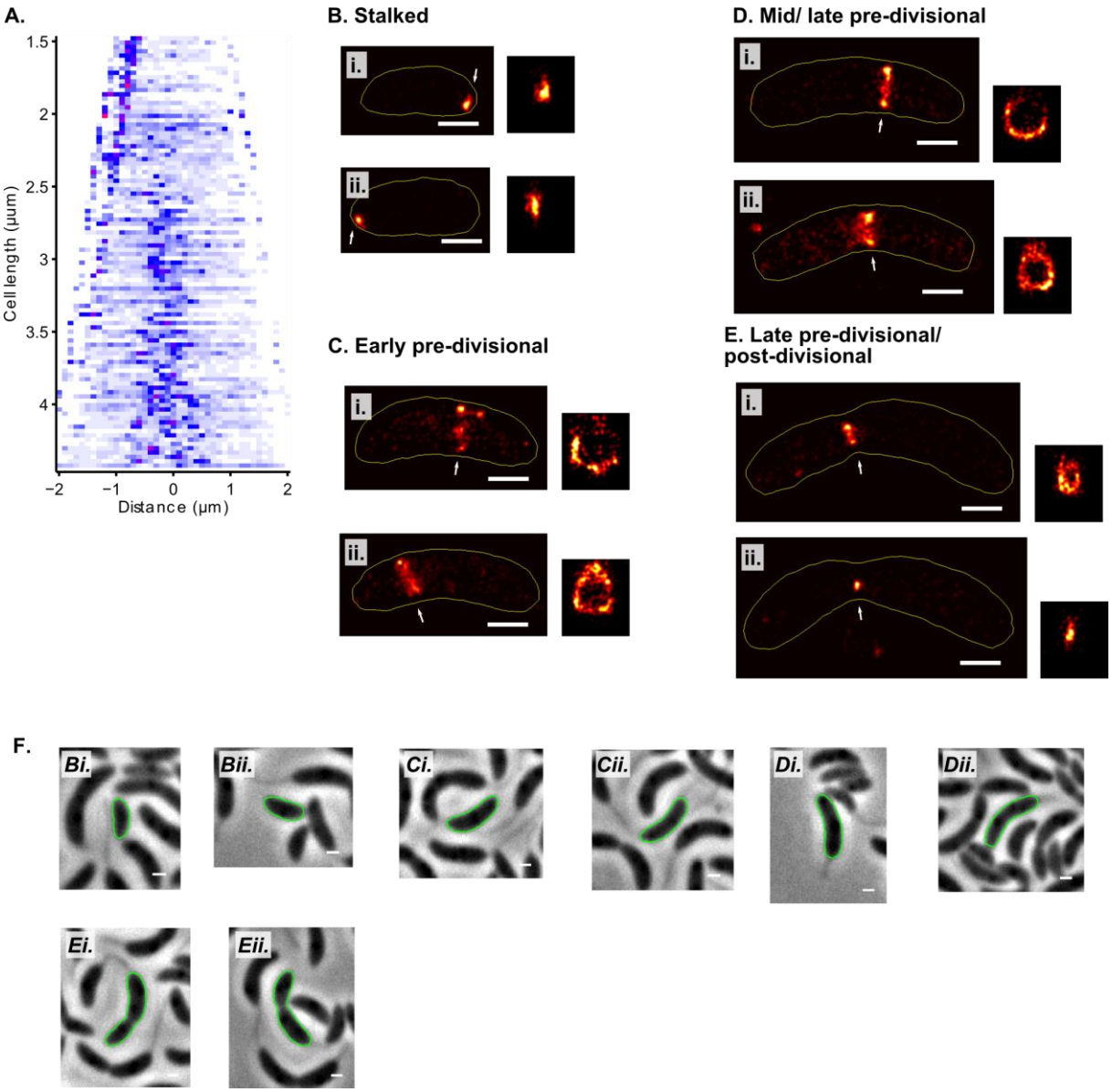

Figure S8: *3D PALM of live, non-synchronized cells imaged at higher speed (20 s/ image)*. *A.* FtsZ axial localization relative to cell centre as a function of time, for 292 cells. *Colormap*: white (lowest density)-blue-red (highest density). *B-E.* Representative PALM images of FtsZ localization throughout the cell cycle, in *xy* (left) and in *zd* cross-section (right), where *d* is lateral displacement from cell mid-plane. Arrow indicates region shown in z-cross-section. Yellow line indicates cell outline, automatically determined from a phase contrast image. *F.* corresponding phase contrast images. Scale bars, 500 nm

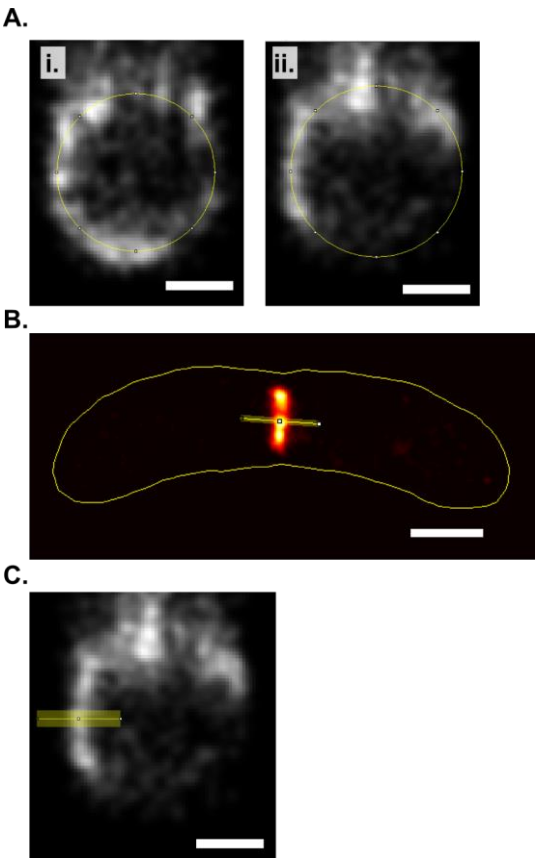

Figure S9: *Examples of manual measurements of ring diameter (A), axial ring thickness (B), and radial ring thickness (C).* Scalebars: z cross-sections (A, C), 200 nm; xy plot (B), 500 nm.

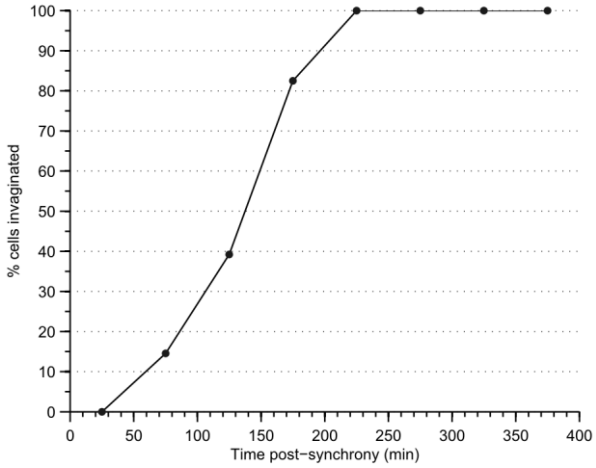

Figure S10: *Percentage of bacteria with visible invagination for dataset in Fig. 4 (n=275).*

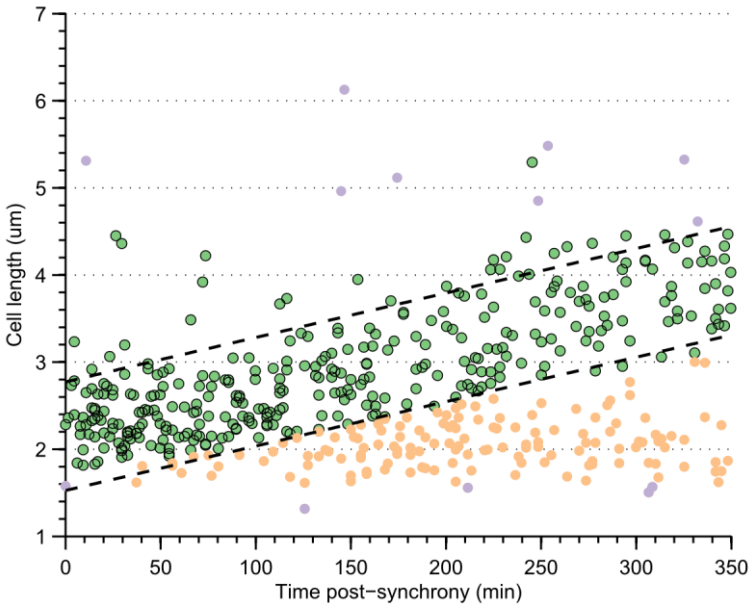

Figure S11: *Length of synchronized cells. Grey circles* indicate cells excluded from analysis due to automated shape-based filtering. *Orange circles* indicate cells which failed to elongate post-synchrony; these (presumably dead) cells were excluded from analysis. *Green circles* indicate cells that passed these thresholds and show the diversity of lengths for healthy, well-segmented cells post synchrony. To maximize the quality of synchronization, cells with a length greater than 1.5 standard deviations from the filtered population (green circles) data were excluded. *Black lines* indicate the running 1.5 s.d. bounds calculated via a linear fit to the filtered population; cells within this range were used for the final analysis.

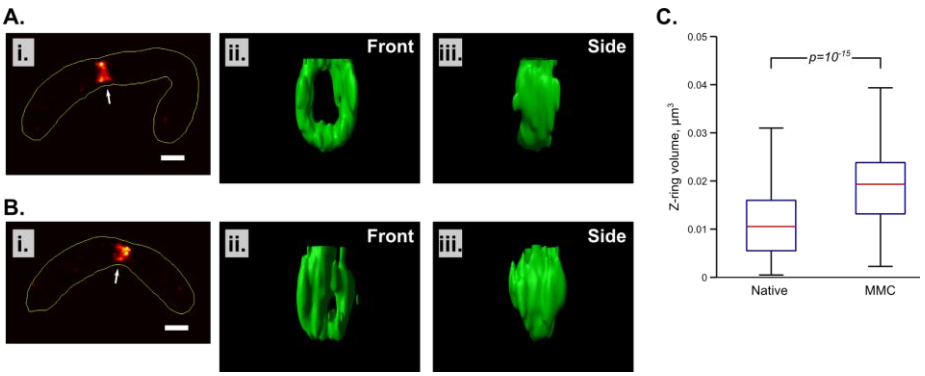

Figure S12: *DNA damage induces formation of high-density, complete Z-rings which are axially extended. A-B.* FtsZ localization after growth in the presence of mitomycin C for > 5 hours. Arrow indicates region shown as 3D volume. Scale bars, 500 nm. Corresponding phase contrast images shown in Fig. S3. *C.* Z-ring volume measurements for native *(n=188)* and MMC treated cells *(n=124).*

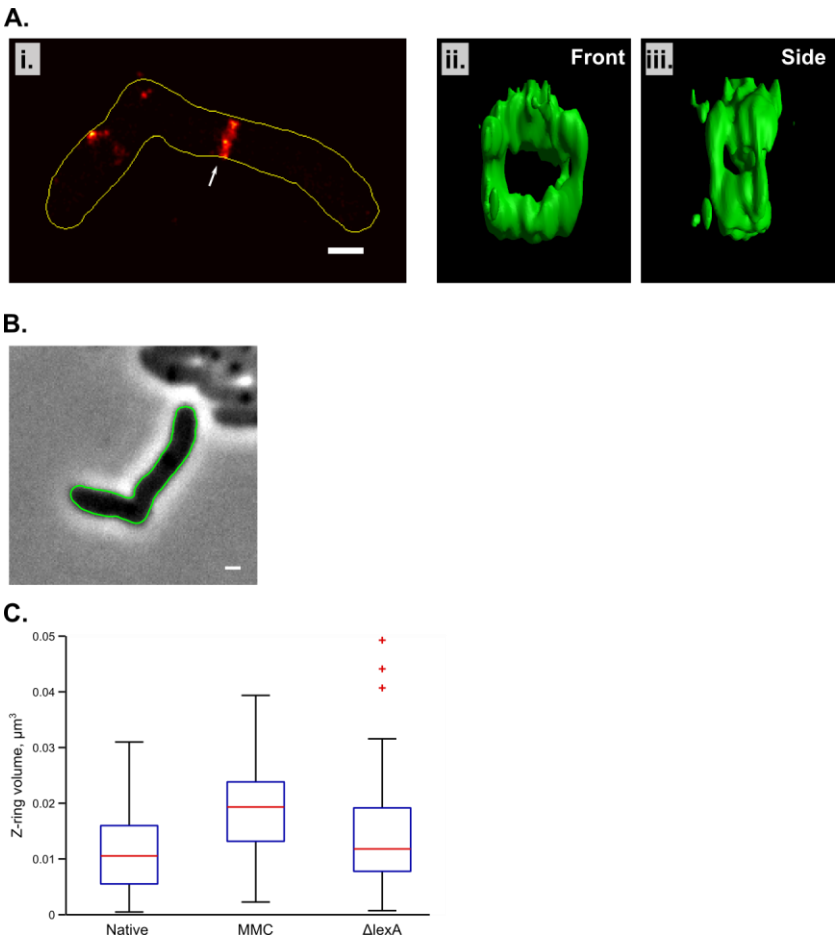

Figure S13: *Z-ring morphology of lexA-deficient cells.* A. 2D (i) and 3D (ii, iii) FtsZ localization. Arrow indicates region shown as 3D volume**.** *B.* Phase contrast image of cell shown in *A. C.* Z-ring volume measurements for native *(n=188,* as per Fig. S12*)*, MMC treated cells *(n=124,* as per Fig. S12*)*, and *ΔlexA* cells (*n=60).* Red crosses, outliers. *p-values* for statistical significance of difference to native condition (Mann-Whitney-Wilcoxon test): MMC treated cells, $p=10^{-15}$, *ΔlexA* cells, *p=0.07.*

Supplementary Tables

	Condition	Number of molecules
Synchronized *C. crescentus*, Xylose 0.003%, 80s acquisition time	Entire cell, xy view, *all cells*	1385 ± 553
	Z-ring, xz view, *all cells*	849 ± 394
	Fig. 2Bi., entire cell, xy view	2006
	Fig. 2Bi., Z-ring, xz view	1429
	Fig. 2Bii., entire cell, xy view	1288
	Fig. 2Bii., Z-ring, xz view	577
	Fig. 2Ci., entire cell, xy view	1711
	Fig. 2Ci., Z-ring, xz view	1034
	Fig. 2Cii., entire cell, xy view	1367
	Fig. 2Cii., Z-ring, xz view	885
	Fig. 2Di., entire cell, xy view	2119
	Fig. 2Di., Z-ring, xz view	1730
	Fig. 2Dii., entire cell, xy view	1775
	Fig. 2Dii., Z-ring, xz view	1354
	Fig. 2E., entire cell, xy view	1473
	Fig. 2E., Z-ring, xz view	894
	Fig. 3Ai, Z-ring, volume rendering (also Fig. S6Ai, xz view)	414
	Fig. 3Aii, Z-ring, volume rendering (also Fig. S6Aii, xz view)	1034
	Fig. 3Aiii, Z-ring, volume rendering (also Fig. S6Aiii, xz view)	679
	Fig. 3Aiv, Z-ring, volume rendering (also Fig. S6Aiv, xz view)	885
	Fig. 3Av, Z-ring, volume rendering (also Fig. S6Av, xz view)	1500
	Fig. 3Bi, Z-ring, volume rendering (also Fig. S6Bi, xz view)	650
	Fig. 3Bii, Z-ring, volume rendering (also Fig. S6Bii, xz view)	1730
	Fig. 3Biii, Z-ring, volume rendering (also Fig. S6Biii, xz view)	792
	Fig. 3Biv, Z-ring, volume rendering (also Fig. S6Biv, xz view)	1007
	Fig. 3Bv, Z-ring, volume rendering (also Fig. S6Bv, xz view)	1122
Synchronized MMC treated *C. crescentus*, Xylose 0.003%, 80s acquisition time	Entire cell, xy view, *all cells*	2294 ± 673
	Z-ring, xz view, *all cells*	1333 ± 373
	Fig. S12Ai, entire cell, xy view	3552
	Fig. S12Aii-iii, entire cell, volume rendering	2252
	Fig. S12Bi, entire cell, xy view	1768
	Fig. S12Bii-iii, entire cell, volume rendering	1208

Un-synchronized *C. crescentus*, Xylose 0.003%, 20s acquisition time	Entire cell, xy view, *all cells*	417 ± 312
	Z-ring, xz view, *all cells*	205 ± 157
	Fig. S8Bi, entire cell, xy view	367
	Fig. S8Bi, Z-ring, xz view	309
	Fig. S8Bii, entire cell, xy view	419
	Fig. S8Bii, Z-ring, xz view	318
	Fig. S8Ci., entire cell, xy view	364
	Fig. S8Ci., Z-ring, xz view	257
	Fig. S8Cii., entire cell, xy view	693
	Fig. S8Cii., Z-ring, xz view	480
	Fig. S8Di., entire cell, xy view	408
	Fig. S8Di., Z-ring, xz view	321
	Fig. S8Dii., entire cell, xy view	771
	Fig. S8Dii., Z-ring, xz view	450
	Fig. S8Ei., entire cell, xy view	484
	Fig. S8Ei., Z-ring, xz view	284
	Fig. S8Eii., entire cell, xy view	297
	Fig. S8Eii., Z-ring, xz view	115
Un-synchronized *C. crescentus*, Xylose 0.015%, 80s acquisition time	Entire cell, xy view, *all cells*	859 ± 636
	Z-ring, xz view, *all cells*	490 ± 361
	Fig. S4B, entire cell, xy view	1091
	Fig. S4B, Z-ring, xz view	985
	Fig. S4Ci., entire cell, xy view	477
	Fig. S4Ci., Z-ring, xz view	385
	Fig. S4Cii., entire cell, xy view	535
	Fig. S4Cii., Z-ring, xz view	390
	Fig. S4Di., entire cell, xy view	1410
	Fig. S4Di., Z-ring, xz view	1029
	Fig. S4Dii., entire cell, xy view	954
	Fig. S4Dii., Z-ring, xz view	606
	Fig. S4E., entire cell, xy view	624
	Fig. S4E., Z-ring, xz view	396
Un-synchronized ΔlexA *C crescentus*, Xylose 0.003%, 80s acquisition time	Entire cell, xy view, *all cells*	2042 ± 1642
	Z-ring, xz view, *all cells*	996 ± 699
	Fig. S13Ai, entire cell, xy view	4664
	Fig. S13Aii,iii, Z-ring	1883

Supplementary Table 1: *Number of localized fluorophores for each dataset, and each figure.* ± indicates 1 s.d.